A perfectly matched layer for fluid-solid problems: Application to ocean-acoustics simulations with solid ocean bottoms

Zhinan Xie[a)]
Institute of Engineering Mechanics, China Earthquake Administration, Harbin 150080, China

René Matzen
Department of Mechanical Engineering, Solid Mechanics, Technical University of Denmark, DK-2800 Kgs. Lyngby, Denmark

Paul Cristini and Dimitri Komatitsch[b)]
LMA, CNRS UPR 7051, Aix-Marseille University, Centrale Marseille, 13453 Marseille cedex 13, France

Roland Martin
GET, CNRS UMR 5563, Université Toulouse III Paul Sabatier, Observatoire Midi-Pyrénées, 14 avenue Édouard Belin, 31400 Toulouse, France

(Received 30 September 2015; revised 2 May 2016; accepted 6 June 2016; published online 11 July 2016)

A time-domain Legendre spectral-element method is described for full-wave simulation of ocean acoustics models, i.e., coupled fluid-solid problems in unbounded or semi-infinite domains, taking into account shear wave propagation in the ocean bottom. The technique can accommodate range-dependent and depth-dependent wave speed and density, as well as steep ocean floor topography. For truncation of the infinite domain, to efficiently absorb outgoing waves, a fluid-solid complex-frequency-shifted unsplit perfectly matched layer is introduced based on the complex coordinate stretching technique. The complex stretching is rigorously taken into account in the derivation of the fluid-solid matching condition inside the absorbing layer, which has never been done before in the time domain. Two implementations are designed: a convolutional formulation and an auxiliary differential equation formulation because the latter allows for implementation of high-order time schemes, leading to reduced numerical dispersion and dissipation, a topic of importance, in particular, in long-range ocean acoustics simulations. The method is validated for a two dimensional fluid-solid Pekeris waveguide and for a three dimensional seamount model, which shows that the technique is accurate and numerically long-time stable. Compared with widely used paraxial absorbing boundary conditions, the perfectly matched layer is significantly more efficient at absorbing both body waves and interface waves.
[http://dx.doi.org/10.1121/1.4954736]

[BTH] Pages: 165–175

I. INTRODUCTION

With the better understanding of the oceanic medium that has occurred over the past decade, the availability of a flexible and highly accurate numerical method, capable of simulating the propagation of acoustic energy in the ocean is becoming necessary in order to take into account increasingly finer ocean scales. Among the numerical methods that can be used to perform such simulations, high-order finite-element methods are candidates of choice because they combine accuracy and flexibility. For instance, in a previous article,[1] the high potential of a spectral-element method for performing numerical simulations in ocean acoustics with various types of rheologies for sediments has been shown. Having the capability of solving, in an efficient way, the full-wave equation in the time domain without any approximation is important for many applications, in particular, configurations in which backscattering or reverberation have an important effect, since such effects cannot accurately be computed by more widely used approaches such as parabolic approximations.[2]

Having such a tool will be an important step towards taking into account the full complexity of the marine environment. Nevertheless, despite the increase in computational power of modern computers, the computational cost of full-wave methods is still high, especially for 3D configurations. One of the reasons for this is the difficulty of implementing efficient absorbing boundary conditions to truncate the computational domain. This is particularly true for long-range ocean acoustics propagation for which computational domains are very elongated. This type of geometry requires an extension of the computational domain in order to avoid contamination of the signals by spurious reflections coming back from its edges. As a consequence, designing an efficient absorbing boundary condition for the full-wave equation in the time domain is of importance because it will

[a)]Also at: LMA, CNRS UPR 7051, Aix-Marseille University, Centrale Marseille, 13453 Marseille cedex 13, France.
[b)]Electronic mail: komatitsch@lma.cnrs-mrs.fr

drastically reduce the computational cost and thus allow one to simulate sources with a much higher frequency content.

Among different numerical techniques designed to minimize the influence of the truncation of the computational domain (see, e.g., Xie *et al.*[3] for a review), perfectly matched layers[4] (PML) and their variants have several nice properties that led to their rapid development in many fields. Several articles used the PML to model wave propagation in ocean acoustics in the frequency domain[5,6] with finite-element methods, in the time domain with finite-difference methods[7,8] or by Fourier synthesis with finite-element methods.[9,10] In all these articles the ocean bottom was assumed to be fluid and thus only fluid PMLs were considered.

In addition to being efficient, this absorbing layer should also be able to handle heterogeneous interfaces. For instance, modeling elasticity in the ocean bottom may be important because shear waves represent a significant loss mechanism due to the conversion of compressional waves that occurs at the interface between water and the sediments. Furthermore, in the case of low-frequency propagation, sources located close to the bottom will lead to the generation of an interface wave that can be prominent. As a consequence, an absorbing layer for realistic ocean acoustic configurations should be able to handle both fluid and elastic media. Heterogeneous PML absorbing layers have been considered in the literature in the frequency domain,[11,12] as well as in the time-domain simulation of propagation in ocean acoustics based on the elastodynamics finite-integration technique.[13] However, to our knowledge no article has addressed heterogeneity of a fluid-solid type in a consistent fashion in the time domain, for which the matching condition inside the boundary layer should take into account the effect of complex stretching,[14] otherwise numerical instabilities can appear. The main purpose of this article is thus to address this problem in order to be able to consider an elastic bottom for wave propagation simulations in ocean acoustics.

This article is a sequel to a previous article[3] dealing with the design of a numerically stable PML for both forward and adjoint simulations, in which the case of time-domain wave propagation in purely elastic domains was addressed. The reader is referred to that article for a review of numerical methods designed to suppress the reflections from the artificial boundaries introduced when truncating semi-infinite or infinite domains. In that article we also derived an auxiliary differential equation (ADE) form of the complex-frequency-shifted unsplit-field perfectly matched layer (CFS-UPML) that allows for extension to higher-order time schemes; we use it again in this article.

The article is organized as follows: Sec. II briefly recalls the basic equations that govern wave propagation in fluid and solid media in the time domain. Section III is devoted to the design of our consistent formulation of PML in coupled fluid-solid domains; we give the strong form and the weak form of this formulation and explain how its numerical implementation can be performed. In Sec. IV we then illustrate its use combined with a spectral-element method in an ocean acoustics context for two dimensional (2D) and three dimensional (3D) configurations.

II. FORMULATION OF THE WAVE EQUATION IN COUPLED FLUID-SOLID DOMAINS

Wave propagation in a lossless linear elastic solid is governed by

$$\begin{aligned} \rho_s \ddot{\mathbf{u}}^s &= \nabla \cdot \boldsymbol{\sigma} + \mathbf{f} \\ \boldsymbol{\sigma} &= \mathbf{c} : \nabla \mathbf{u}^s \end{aligned} \qquad \mathbf{x} \in \Omega_s, \tag{1}$$

where ρ_s is mass density, $\mathbf{u}^s$ represents the spatially varying displacement vector under the hypothesis of small displacements, and $\mathbf{f}$ is the source term. "$\nabla\cdot$" and "∇" denote the divergence and gradient operators, respectively, and a dot over a symbol denotes time differentiation. $\boldsymbol{\sigma}$ is the symmetric second-order stress tensor and $\mathbf{c}$ is the fourth-order constitutive stiffness tensor, whose elements in the case of an isotropic medium are given by

$$c_{ijkl} = \lambda\, \delta_{ij}\delta_{kl} + \mu(\delta_{ik}\delta_{jl} + \delta_{il}\delta_{jk}) \tag{2}$$

(for $i,j,k,l = 1,2,3$) where δ_{ij} is the Kronecker delta, λ is Lamé's first parameter and μ is the shear modulus. The subscript and superscript "s," respectively, indicate the scalar material parameters and state variables of the solid region, whereas for the fluid region we use subscript "f." The medium is initially at rest and thus the initial conditions are

$$\mathbf{u}^s(\mathbf{x},0) = \dot{\mathbf{u}}^s(\mathbf{x},0) = 0 \quad \mathbf{x} \in \Omega_s. \tag{3}$$

The traction-free boundary condition along the elastic surface $\partial\Omega_s$ reads

$$\boldsymbol{\sigma} \cdot \mathbf{n} = 0 \quad \mathbf{x} \in \partial\Omega_s, \tag{4}$$

and continuity conditions at solid-solid interfaces are

$$\begin{aligned} [\mathbf{u}^s]^+_- &= 0 \\ [\boldsymbol{\sigma} \cdot \mathbf{n}]^+_- &= 0 \end{aligned} \qquad \mathbf{x} \in \Gamma_s, \tag{5}$$

where the vector $\mathbf{n}$ represents the normal to the surface and $[\,\cdot\,]^+_-$ denotes the jump of the quantity enclosed across the oriented surface Γ_{ab} separating domains Ω_a and Ω_b. The normal $\mathbf{n}$ to the surface is defined at the boundary Γ_{ab} with an orientation from the boundary of domain Ω_a pointing into domain Ω_b.

Inside the fluid region Ω_f considered as an inviscid fluid and with small displacement perturbations, first-order momentum conservation writes[15]

$$\rho_f \ddot{\mathbf{u}}^f = -\nabla p, \tag{6}$$

where ρ_f is the spatially varying mass density of the hydrostatic state, $\mathbf{u}^f$ is the displacement of the fluid particle, and p denotes the hydrodynamic pressure. The continuity equation relates pressure to displacement by[15]

$$\dot{p} = -\kappa \nabla \cdot \dot{\mathbf{u}}^f, \tag{7}$$

where $\kappa = \rho_f c^2$ is the bulk modulus and c is the sound speed. One can alternatively introduce a displacement potential χ related to pressure:

$$p = -\ddot{\chi}, \tag{8}$$

which yields

$$\mathbf{u}^f = \rho_f^{-1}\nabla\chi. \tag{9}$$

The stress tensor inside the fluid is then $\boldsymbol{\sigma} = -p\mathbf{I} = \ddot{\chi}\mathbf{I}$ with $\mathbf{I}$ denoting the identity tensor, and one gets the second-order scalar acoustic wave equation:

$$\kappa^{-1}\ddot{\chi} = \nabla\cdot(\rho_f^{-1}\nabla\chi) + \kappa^{-1}q, \quad \mathbf{x}\in\Omega_f, \tag{10}$$

where q has been added to represent a pressure source in the fluid region, such as an underwater air-gun or explosion. The initial conditions are

$$\chi(\mathbf{x},0) = \dot{\chi}(\mathbf{x},0) = 0, \quad \mathbf{x}\in\Omega_f. \tag{11}$$

The traction-free condition at the surface of the fluid is then

$$\chi = \dot{\chi} = 0, \quad \mathbf{x}\in\partial\Omega_f, \tag{12}$$

and continuity conditions at fluid-fluid interfaces are

$$\begin{aligned}[\chi\cdot\mathbf{n}]_-^+ &= 0\\ [\bar{\mathbf{u}}^f\cdot\mathbf{n}]_-^+ &= 0\end{aligned} \quad \mathbf{x}\in\Gamma_f. \tag{13}$$

The strong form for the physical problem is finally completed by ensuring coupling along the fluid-solid interface Γ_{fs} through a matching of the traction vector as well as of the normal component of displacement (only):

$$\begin{aligned}\boldsymbol{\sigma}\cdot\mathbf{n} &= \ddot{\chi}\mathbf{n}\\ \mathbf{u}^s\cdot\mathbf{n} &= \mathbf{u}^f\cdot\mathbf{n}\end{aligned} \quad \mathbf{x}\in\Gamma_{fs}. \tag{14}$$

III. CFS-UPML EQUATIONS FOR FLUID-SOLID DOMAIN TRUNCATION

A. Strong form in the frequency domain

Following the classical approach of complex coordinate stretching in the PML (Ref. 16) the real coordinate component x_i is stretched by a general complex coordinate-wise function $s_i(x_i)$ such that the stretched Cartesian coordinate $\tilde{x}_i$ is defined by

$$\tilde{x}_i(x_i) = \int_0^{x_i} s_i(u)\,\mathrm{d}u \tag{15}$$

(for i = 1,2,3). In order to enhance absorption for evanescent waves, as well as waves at grazing incidence, one usually adopts the CFS-enriched stretching function:[17]

$$s_i(x_i) = \kappa_i(x_i) + \frac{d_i(x_i)}{\alpha_i(x_i) + \mathrm{i}\omega} \tag{16}$$

(no summation), where ω is the angular frequency and $\mathbf{i}$ denotes the imaginary unit number. Inside the PML along the normal direction x_i, d_i is a damping factor that makes the amplitude of an outgoing wave field propagating with arbitrary angles of incidence decay exponentially, α_i denotes the factor that makes the damping rate frequency dependent, effectively implementing a Butterworth-type filter in addition to PML, and κ_i is a scaling factor that enhances the attenuation of evanescent waves. One can refer to, e.g., Zhang and Shen[14] for a more precise analysis of the meaning of d_i, α_i, and κ_i.

Considering the solid and fluid wave Eqs. (1) and (10) in the frequency domain, in Cartesian coordinates the new stretched gradient is introduced through the chain rule as

$$\tilde{\nabla} = (s_1s_2s_3)^{-1}\widehat{\mathbf{M}}\cdot\nabla, \tag{17}$$

where $\widehat{\mathbf{M}}$ is a diagonal second-order tensor with elements $\widehat{M}_{ij} = \delta_{ij}(s_1s_2s_3/s_i)$ (no summation).

For the surface normal $\mathbf{n}$ in the boundary conditions in Eqs. (4), (5), and (14) we use the fact that the normal on any regular and orientable surface Γ implicitly represented by $F(x_1,x_2,x_3) = 0$ is given by $\mathbf{n} = \nabla F(x_1,x_2,x_3)$ to obtain its stretched counterpart:[18]

$$\tilde{\mathbf{n}} = (s_1s_2s_3)^{-1}\widehat{\mathbf{M}}\cdot\mathbf{n}. \tag{18}$$

Next, substituting the stretched gradient operator in Eq. (17) into the stretched wave equation in the frequency domain and using the identity $(\widehat{\mathbf{M}}\cdot\nabla)\cdot\mathbf{T} = \nabla\cdot(\widehat{\mathbf{M}}\cdot\mathbf{T})$ for any tensor $\mathbf{T}$, the strong form of the wave equation for the coupled fluid-solid problem without external sources reads[3,19]

$$\begin{aligned}-\rho_s s_1s_2s_3\omega^2\widehat{\mathbf{u}}^s &= \nabla\cdot\widehat{\boldsymbol{\sigma}}\\ \widehat{\boldsymbol{\sigma}} &= \widehat{\mathbf{c}}:\nabla\widehat{\mathbf{u}}^s\end{aligned} \quad \mathbf{x}\in\Omega_s^{\mathrm{PML}}, \tag{19}$$

$$\begin{aligned}-\kappa^{-1}s_1s_2s_3\omega^2\widehat{\chi} &= \nabla\cdot\widehat{\mathbf{u}}^f\\ \widehat{\mathbf{u}}^f &= \widehat{\rho}\cdot\nabla\widehat{\chi}\end{aligned} \quad \mathbf{x}\in\Omega_f^{\mathrm{PML}}, \tag{20}$$

where we have multiplied by the Jacobian $J = |\partial\tilde{x}_i/\partial x_j| = s_1s_2s_3$ on the two sides of the equations. Substituting the stretched surface normal in Eq. (18) into the stretched boundary and coupling conditions then gives

$$\widehat{\boldsymbol{\sigma}}\cdot\mathbf{n} = 0, \quad \mathbf{x}\in\partial\Omega_s^{\mathrm{PML}}, \tag{21}$$

$$\begin{aligned}[\widehat{\boldsymbol{\sigma}}\cdot\mathbf{n}]_-^+ &= 0\\ [\widehat{\mathbf{u}}^s]_-^+ &= 0\end{aligned} \quad \mathbf{x}\in\Gamma_s^{\mathrm{PML}}, \tag{22}$$

$$\chi = \dot{\chi} = 0, \quad \mathbf{x}\in\partial\Omega_f^{\mathrm{PML}} \tag{23}$$

$$\begin{aligned}[(\widehat{\mathbf{N}}\widehat{\chi})\cdot\mathbf{n}]_-^+ &= 0\\ [\widehat{\mathbf{u}}^f\cdot\mathbf{n}]_-^+ &= 0\end{aligned} \quad \mathrm{X}\in\Gamma_f^{\mathrm{PML}}, \tag{24}$$

$$\begin{aligned}\widehat{\boldsymbol{\sigma}}\cdot\mathbf{n} &= (\widehat{\mathbf{N}}\widehat{\chi})\cdot\mathbf{n}\\ (\widehat{\mathbf{M}}\cdot\widehat{\mathbf{u}}^s)\cdot\mathbf{n} &= \widehat{\mathbf{u}}^f\cdot\mathbf{n}\end{aligned} \quad \mathbf{x}\in\Gamma_{fs}^{\mathrm{PML}}, \tag{25}$$

where $\widehat{c}_{ijkl} = c_{ijkl}(s_1s_2s_3/s_is_k)$ and $\widehat{\rho}_{ij} = \rho_f^{-1}\delta_{ij}(s_1s_2s_3/s_is_j)$ (no summation) are stretched material parameters, and $\widehat{\mathbf{N}} = -\omega^2\widehat{\mathbf{M}}$. The "$\widehat{\ }$" and "$\_$" symbols indicate the frequency-domain and stretched expressions, respectively. It is worth mentioning that in order to be consistent with the

wave equation and be able to use Gauss's theorem, one needs to multiply by the Jacobian $J = s_1 s_2 s_3$ on both sides of the above equations that describe the boundary and interface conditions. Using such a complex-stretching approach to derive the PML is classical.[19–21] Recently, Matuszyk and Demkowicz[11] have reinterpreted the complex-stretching technique in terms of complex Piola-like transforms, and by applying such transforms to the weak form of the fluid-solid wave equation they obtained the weak-form fluid-solid PML and the corresponding matching condition in the frequency domain.

B. Strong form in the time domain

The time-domain counterpart of the above strong form of the governing equations is obtained by using the inverse Fourier transform, which yields

$$\begin{aligned} &\rho_s L(t) * \mathbf{u}^s = \nabla \cdot \bar{\boldsymbol{\sigma}} \\ &\bar{\boldsymbol{\sigma}} = \bar{\mathbf{C}}(t) : \nabla \mathbf{u}^s \end{aligned} \qquad \mathbf{x} \in \Omega_s^{\mathrm{PML}}, \tag{26}$$

$$\begin{aligned} &\kappa^{-1} L(t) * \chi = \nabla \cdot \bar{\mathbf{u}}^f \\ &\bar{\mathbf{u}}^f = \bar{\mathbf{P}}(t) \cdot \nabla \chi \end{aligned} \qquad \mathbf{x} \in \Omega_f^{\mathrm{PML}}, \tag{27}$$

subjected to the boundary and coupling conditions:

$$\bar{\boldsymbol{\sigma}} \cdot \mathbf{n} = 0, \quad \mathbf{x} \in \partial\Omega_s^{\mathrm{PML}}, \tag{28}$$

$$\begin{aligned} &[\bar{\boldsymbol{\sigma}} \cdot \mathbf{n}]_-^+ = 0 \\ &[\mathbf{u}^s]_-^+ = 0 \end{aligned} \qquad \mathbf{x} \in \Gamma_s^{\mathrm{PML}}, \tag{29}$$

$$\chi = \dot{\chi} = 0, \quad \mathbf{x} \in \partial\Omega_f^{\mathrm{PML}}, \tag{30}$$

$$\begin{aligned} &[(\mathbf{N}(t) * \chi) \cdot \mathbf{n}]_-^+ = 0 \\ &[\bar{\mathbf{u}}^f \cdot \mathbf{n}]_-^+ = 0 \end{aligned} \qquad \mathbf{x} \in \Gamma_f^{\mathrm{PML}}, \tag{31}$$

$$\begin{aligned} &\bar{\boldsymbol{\sigma}} \cdot \mathbf{n} = [\mathbf{N}(t) * \chi] \cdot \mathbf{n} \\ &[\mathbf{M}(t) * \mathbf{u}^s] \cdot \mathbf{n} = \bar{\mathbf{u}}^f \cdot \mathbf{n} \end{aligned} \qquad \mathbf{x} \in \Gamma_{fs}^{\mathrm{PML}}, \tag{32}$$

where $L(t) = \mathcal{F}^{-1}[-\omega^2 s_1 s_2 s_3]$ and where the elements of $\bar{\mathbf{C}}(t)$, $\bar{\mathbf{P}}(t)$, $\mathbf{M}(t)$, and $\mathbf{N}(t)$ are $\bar{C}_{ijkl} = c_{ijkl}\mathcal{F}^{-1}[s_1 s_2 s_3 / s_i s_k]$, $\bar{P}_{ij} = \rho_f^{-1}\delta_{ij}\mathcal{F}^{-1}[s_1 s_2 s_3 / s_i s_j]$, $M_{ij} = \delta_{ij}\mathcal{F}^{-1}[s_1 s_2 s_3 / s_i]$, and $N_{ij} = \delta_{ij}\mathcal{F}^{-1}[-\omega^2 (s_1 s_2 s_3 / s_i)]$ (no summation). The use of capital letters for material tensor representation in tensor and dot products indicates that multiplication is replaced by convolution, i.e., $\bar{\mathbf{C}}(t) : \nabla \mathbf{u} = \bar{C}_{ijkl}(t) * \nabla_k u_l$ and $\bar{\mathbf{P}}(t) \cdot \nabla \chi = \bar{P}_{ij}(t) * \nabla_j \chi$.

C. Weak form in the time domain

The weak form of these equations is then obtained by associating spatially dependent test functions $\mathbf{w}$ and w with the solid displacement $\mathbf{u}^s$ and the acoustic displacement potential χ, respectively. They inherit the boundary conditions from the physical fields. Then, by dotting or multiplying the CFS-UPML strong formulations of the solid and fluid wave Eqs. (26) and (27) with $\mathbf{w}$ and with w, respectively, integrating the resulting set of equations by parts in the region $\Omega_{fs}^{\mathrm{PML}} = \Omega_f^{\mathrm{PML}} \cup \Omega_s^{\mathrm{PML}}$ (see Fig. 1), and invoking Gauss's theorem, the weak formulation is obtained and the

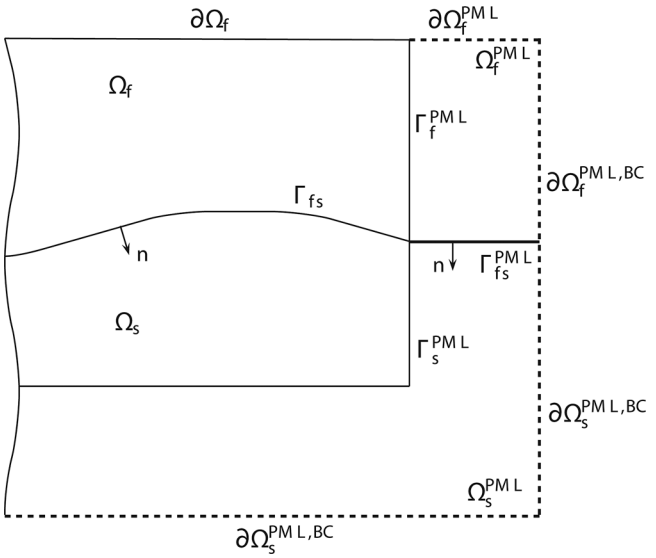

FIG. 1. Setup of the problem under study: The physical fluid-solid region $\Omega_{fs} = \Omega_f \cup \Omega_s$, separated by Γ_{fs}, is truncated by the PML $\Omega_{fs}^{\mathrm{PML}} = \Omega_f^{\mathrm{PML}} \cup \Omega_s^{\mathrm{PML}}$ that is separated by the fluid-solid interface $\Gamma_{fs}^{\mathrm{PML}}$ and with outer boundary $\partial\Omega_{fs}^{\mathrm{PML}} = \partial\Omega_f^{\mathrm{PML}} \cup \partial\Omega_f^{\mathrm{PML,BC}} \cup \partial\Omega_s^{\mathrm{PML,BC}}$. The computational domain has a traction-free boundary along its surface $\partial\Omega_f \cup \partial\Omega_f^{\mathrm{PML}}$, and also along the outer edges of the fluid PML $\partial\Omega_f^{\mathrm{PML,BC}}$, where $\chi = 0$. Rigid conditions (null displacement) are set along the outer edges of the solid PML $\partial\Omega_s^{\mathrm{PML,BC}}$.

problem to be solved consists in finding the solutions $\mathbf{u}^s$ and χ of the system of equations:

$$\begin{aligned} &\int_{\Omega_f^{\mathrm{PML}}} \kappa^{-1} w\,[L(t) * \chi]\,\mathrm{d}^3\mathbf{x} + \int_{\Omega_f^{\mathrm{PML}}} \nabla w \cdot \bar{\mathbf{u}}^f\,\mathrm{d}^3\mathbf{x} \\ &\quad = \int_{\Gamma_{fs}^{\mathrm{PML}}} w\,(\bar{\mathbf{u}}^f \cdot \mathbf{n})\,\mathrm{d}^2\mathbf{x} + \int_{\partial\Omega_f^{\mathrm{PML}}} w\,(\bar{\mathbf{u}}^f \cdot \mathbf{n})\,\mathrm{d}^2\mathbf{x}, \end{aligned} \tag{33}$$

$$\begin{aligned} &\int_{\Omega_s^{\mathrm{PML}}} \rho_s \mathbf{w}\,[L(t) * \mathbf{u}^s]\,\mathrm{d}^3\mathbf{x} + \int_{\Omega_s^{\mathrm{PML}}} \nabla \mathbf{w} : \bar{\boldsymbol{\sigma}}\,\mathrm{d}^3\mathbf{x} \\ &\quad = \int_{\Gamma_{fs}^{\mathrm{PML}}} \mathbf{w} \cdot (-\bar{\boldsymbol{\sigma}} \cdot \mathbf{n})\,\mathrm{d}^2\mathbf{x} + \int_{\partial\Omega_s^{\mathrm{PML}}} \mathbf{w} \cdot (\bar{\boldsymbol{\sigma}} \cdot \mathbf{n})\,\mathrm{d}^2\mathbf{x}, \end{aligned} \tag{34}$$

where $w \in H^1(\Omega_f^{\mathrm{PML}})$ and $\mathbf{w} \in H^1(\Omega_s^{\mathrm{PML}})$. The spaces $H^1(\Omega_f^{\mathrm{PML}})$ and $H^1(\Omega_s^{\mathrm{PML}})$ denote, respectively, the space of scalar fields or vector fields defined on Ω_f^{PML} or Ω_s^{PML} that are square integrable and have square-integrable first-order partial derivatives in space over the domain Ω_f^{PML} or Ω_s^{PML}. The test functions w and $\mathbf{w}$ satisfy the same set of boundary conditions as χ and $\mathbf{u}^s$. The integral on the right-hand side of Eqs. (33) or (34) along Γ_f^{PML} or Γ_s^{PML}, respectively, cancels out with its counterpart in the weak form of the wave equation in the physical region owing to the perfectly matched property of PML. Such a property can be proven using reflection-coefficient analysis[22] based on the fact that the CFS-UPML equation shares the same closed-form solution as the wave equation in the physical region.[23] The same integral along the outer edge of the PML $\partial\Omega_f^{\mathrm{PML,BC}}$ or $\partial\Omega_s^{\mathrm{PML,BC}}$ is also equal to zero because we impose Dirichlet boundary conditions there:

$$\chi = \dot{\chi} = 0, \quad \mathbf{x} \in \partial\Omega_f^{\mathrm{PML,BC}}, \tag{35}$$

$$\mathbf{u}^s = \dot{\mathbf{u}}^s = 0, \quad \mathbf{x} \in \partial\Omega_s^{\mathrm{PML,BC}}. \tag{36}$$

Applying the boundary conditions in Eqs. (28)–(32), the weak form finally becomes

$$\int_{\Omega_f^{\mathrm{PML}}} \kappa^{-1} w\,[L(t) * \chi]\,\mathrm{d}^3\mathbf{x} + \int_{\Omega_f^{\mathrm{PML}}} \nabla w \cdot [\bar{\mathbf{P}}(t) \cdot \nabla\chi]\,\mathrm{d}^3\mathbf{x} = \int_{\Gamma_{fs}^{\mathrm{PML}}} w\,([\mathbf{M}(t) * \mathbf{u}^s] \cdot \mathbf{n})\,\mathrm{d}^2\mathbf{x}, \tag{37}$$

$$\int_{\Omega_s^{\mathrm{PML}}} \rho_s \mathbf{w} \cdot [L(t) * \mathbf{u}^s]\,\mathrm{d}^3\mathbf{x} + \int_{\Omega_s^{\mathrm{PML}}} \nabla\mathbf{w} : [\bar{\mathbf{C}}(t) : \nabla\mathbf{u}^s]\,\mathrm{d}^3\mathbf{x} = \int_{\Gamma_{fs}^{\mathrm{PML}}} \mathbf{w} \cdot ([-\mathbf{N}(t) * \chi]\ \cdot \mathbf{n})\,\mathrm{d}^2\mathbf{x}. \tag{38}$$

To our knowledge such a consistent derivation of the fluid-solid interface conditions inside the PML, taking into account the effect of complex stretching in the derivation of the fluid-solid matching condition, has never been done before in the time domain. Using formal computing software such as Mathematica or Maple, $L(t)$, $\bar{\mathbf{C}}(t)$, $\mathbf{M}(t)$, $\bar{\mathbf{P}}(t)$, and $\mathbf{N}(t)$ can be obtained from their frequency-domain expression based on an inverse Fourier transform. In Xie *et al.*[3] we explicitly considered the fact that the frequency-domain expressions can have singularities in the parameter space spanned by κ_i, α_i, and d_i (for $i = 1, 2, 3$). For first-order singularities a transient growth term te^{-at} then arises in the time-domain expressions, while for second-order singularities that term is t^2e^{-at}. The positive real value a depends on α_i and d_i. Based on numerical experiments we showed that these transient growth terms can trigger numerical instabilities if the singularities are not handled explicitly in the time integration process, as also observed by Kaltenbacher *et al.*[24] In Xie *et al.*[3] we thus introduced a mathematical strategy to handle and remove these singularities. Here we use a simpler approach which consists in selecting the α_i damping profiles in a clever way so that these singularities are completely avoided: since these singularities arise from terms of the type $1/(\alpha_x - \alpha_y)$ for instance, by making sure that α_x and α_y are never equal anywhere in the corners of the PML domains, the singularities never appear; the same must be true for the two other pairs: α_x and α_z, and α_y and α_z.

The convolution terms that appear in the time-domain weak form of Eqs. (37)–(38) all have the following generic form:

$$R_u^a(t) = [e^{-at}H(t)] * u, \tag{39}$$

where $H(t)$ is the unit Heaviside function. In principle these terms involve the entire past history of the medium, which is not realistically possible to store from a computational point of view. Fortunately they can be computed efficiently without having to store the whole simulation history using an incremental recursive convolution technique[3,19,25–27] based on an algebraic property of the convolution kernel $e^{-\alpha_i t}H(t)$:

$$e^{-a(t\pm t_0)}H(t\pm t_0) = e^{-at}e^{\pm at_0} \tag{40}$$

(for $t \pm t_0 \geq 0$) where t_0 is a real constant. However, since that recursive convolution technique can only be implemented to second-order accuracy in time in a straightforward way, the convolution terms of Eq. (39) can alternatively be expressed as being the solution of the following ADE (Refs. 14, 28, and 29):

$$\dot{R}_u^a = \frac{\partial}{\partial t}\left[e^{-at}H(t)\right] * u = \left[-ae^{-at}H(t)\right] * u + \left[e^{-at}\delta(t)\right] * u = -aR_u^a + u, \tag{41}$$

where we have used the fact that the derivative of a Heaviside $H(t)$ is a Dirac $\delta(t)$. The combination of Eqs. (37) and (38) together with the ADE equations governing all the convolution terms results in the time-domain CFS-UPML ADE formulation, in which there are no constraints on the order of the time integration scheme that can be used. Thus, higher-order schemes such as low-dispersion and low-dissipation Runge-Kutta (LDDRK) (Ref. 30) can for instance be employed, thereby increasing the accuracy of simulations that involve a large number of time steps, for which keeping numerical dispersion and dissipation low becomes an important issue.

D. Numerical implementation

In order to solve the coupled set of fluid-solid governing Eqs. (37) and (38), for spatial discretization we resort to the spectral-element method, which is a well-documented technique when it comes to solving acoustic or seismic wave propagation problems.[1,31,32] In order to facilitate a displacement-based time integration scheme we need to resolve the convolution terms in a consistent way. Upon discretization the system of second-order ordinary differential equations reads

$$\mathbf{M}^f\ddot{\mathbf{X}} + \mathbf{C}^f\dot{\mathbf{X}} + \mathbf{M}_{\mathrm{X}}^f\mathbf{X} + \sum_{\cup\Omega_{f,e}^{\mathrm{PML}}} \mathbf{R}_e(\mathbf{X}) + \sum_{\cup\Gamma_{s,e}^{\mathrm{PML}}} \mathbf{R}_e(\mathbf{U}) = \mathbf{F}^{sf}(\mathbf{X}, \mathbf{U}), \tag{42}$$

$$\mathbf{M}^s\ddot{\mathbf{U}} + \mathbf{C}^s\dot{\mathbf{U}} + \mathbf{M}_{\mathrm{U}}^s\mathbf{U} + \sum_{\cup\Omega_{s,e}^{\mathrm{PML}}} \mathbf{R}_e(\mathbf{U}) + \sum_{\cup\Gamma_{f,e}^{\mathrm{PML}}} \mathbf{R}_e(\mathbf{X}) = \mathbf{F}^{fs}(\mathbf{U}, \mathbf{X}), \tag{43}$$

where $\mathbf{U}$ denotes the global nodal vector that collects displacement vector components in the solid part and $\mathbf{X}$ denotes the global scalar potential vector in the fluid part. The forcing term is given by

$$\mathbf{F}^{ab}(\mathbf{X}, \mathbf{Y}) = \sum_{\cup\Omega_{b,e}^{\mathrm{PML}}} \mathbf{K}_e^b(\mathbf{X}) + \sum_{\cup\Gamma_{a,e}^{\mathrm{PML}}} \mathbf{K}_e^{ab}(\mathbf{Y}), \tag{44}$$

where indices a and b can refer to the solid or fluid. $\mathbf{R}_e(\mathbf{A})$ represents an element-level convolution operation on the global vector field $\mathbf{A}$ stemming from the first left-hand side

and the right-hand side integral of Eqs. (37) and (38). For the generic forcing term in Eq. (44), $\mathbf{K}_e^b(\mathbf{X})$ is the element-level stiffness convolution contribution from the second left-hand side integral in Eqs. (37) and (38) in region Ω_b^{PML}, and $\mathbf{K}_e^{ab}(\mathbf{Y})$ contains the fluid-solid coupling condition convolution contribution from the right-hand side integral in Eqs. (37) and (38) that originates from the boundary of region Ω_b and needs to be taken into account on the boundary of Ω_a. In the case of the convolutional formulation of PML we march the spatially discretized governing Eqs. (42) and (43) in time using an explicit, conditionally stable, Newmark time integration scheme, combined with the stabilized recursive convolution scheme derived in Xie *et al.*[3] As a result of the combined effect of applying a scalar displacement potential formulation to capture the fluid field behavior together with explicit time integration, we avoid having to perform iterative sub-steps within each time step for fluid-solid matching.[33] In the case of the ADE formulation of PML we rewrite the system of second-order differential Eqs. (42) and (43) as a first-order system of ordinary differential equations to facilitate high-order temporal integration based on the LDDRK scheme of Berland *et al.*[30]

IV. NUMERICAL RESULTS

In this section we illustrate the accuracy and efficiency of a SEM coupled with our new formulation of CFS-UPML for two ocean acoustics configurations with an elastic bottom. The first configuration is a 2D elastic Pekeris waveguide model of shallow water propagation, while the second corresponds to a less elongated model of a 3D seamount with a source located close to the bottom and leading to the generation of a surface wave of Stoneley-Scholte type at the fluid-solid interface.

Unless otherwise specified, in all examples we use a polynomial degree $N = 4$ for the Lagrange interpolants inside each spectral element. Regarding time discretization we use the LDDRK scheme for the ADE formulation of CFS-UPML in the 2D example, while in the 3D case we use the Newmark time scheme coupled with our second-order convolution scheme of the convolution formulation of CFS-UPML. Following Collino and Tsogka,[22] in the PML coordinate stretching function of Eq. (16) we define d_{x_i} as

$$d_{x_i} = C_{x_i} d_0 \left(\frac{x_i}{L_{x_i}}\right)^{N_{x_i}}, \tag{45}$$

where L_{x_i} is the thickness of the PML along the x_i direction, x_i is the distance along the normal direction measured from the entrance of the PML, N_{x_i} is a real number greater than 1, and

$$d_0 = -(N_{x_i} + 1) c_p^{\max} \log(R_c)/(2L_{x_i}). \tag{46}$$

The values of N_{x_i}, C_{x_i}, R_c can be optimized to obtain good absorption[34] and thus here we set $N_{x_i} = 2$, $C_{x_i} = 1$, $R_c = 0.001$ accordingly. Following a slightly modified version of Gedney[34] we also set

$$\alpha_{x_i} = \pi f_0 \left(1 - \frac{x_i}{L_{x_i}} + t_i\right), \tag{47}$$

where f_0 is the dominant frequency of the source and where t_i is a very small shifting parameter that we use to make sure that terms such as $1/(\alpha_{x_i} - \alpha_{x_j})$ are never equal in the corners of the PML, as explained above. The advantages and disadvantages of using a varying κ_{x_i} are discussed in detail in Zhang and Shen.[14] The main advantage is that it makes CFS-UPML more efficient at absorbing grazing-incidence waves, but a disadvantage is that it slightly decreases the absorbing efficiency for normal or near-normal incidence waves. In practice we thus always choose values of κ_{x_i} lower than five at the end of the PML. Since to our knowledge no optimized profile of κ_{x_i} is discussed in the literature we simply define κ_{x_i} as

$$\kappa_{x_i} = \kappa_0 + \kappa_1 \frac{x_i}{L_{x_i}}, \tag{48}$$

where κ_0 and κ_1 are positive real numbers, with $\kappa_0 \geq 1$. In the following examples we set $\kappa_0 = 1$ and $\kappa_1 = 1$.

A. 2D elastic Pekeris waveguide

The Pekeris waveguide[35] is the simplest model that, despite its simplicity, has all the main characteristic properties of wave propagation in shallow water. It has thus been extensively studied over the past decades. This reference model, which consists of an iso-velocity water column overlying a semi-infinite, sediment fluid bottom, was later extended by Press and Ewing[36] in order to include shear waves in the ocean bottom. In this section we consider such a waveguide by assuming a bottom of a wet sand type having slow shear-wave velocity. In general, the geometry of shallow water propagation models is such that the vertical and horizontal dimensions are very different: typically, the water layer thickness is a few hundred meters while the propagation range can be several kilometers. This leads to very elongated models for which the use of a PML to accurately mimic a semi-infinite bottom is crucial.

This section is devoted to the analysis of the benefits of adding a PML on the modal structure of the wavefield in a shallow water waveguide. For this purpose, we consider a shallow water waveguide for which the water layer thickness is on the order of a few wavelengths. In this configuration, the wavefield can be expressed as a finite sum of modes plus a branch line integral.[35] Several authors[37–40] have investigated the problem of replacing the semi-infinite fluid bottom with a layer of finite size to which a PML is added. They studied how adding a PML modifies the eigenvalue spectrum of the original problem. All these studies show that the approximate model provides a very good approximation to the original one, but only Lu and Zhu[38] address the case in which a mode is close to its cutoff frequency, and they thus expect a large side effect due to the presence of the PML in that case. Since all these studies were performed in the frequency domain, very little attention was paid to this particular case; but performing time-domain simulations makes this

difficulty much more pronounced because in this case many frequencies are excited and several of them can be equal to the cutoff frequency of a propagative mode.

In this section, we consider a 2D elastic Pekeris waveguide whose characteristics are given in Table I. Since the sediment shear wave speed is lower than the water sound speed, there is only one critical angle and this configuration will have characteristics close to a configuration with a fluid sediment bottom. We will consider long range propagation. As a consequence, evanescent modes will not contribute to the sound field, and in the vicinity of the source evanescent waves will be efficiently attenuated by the PML thanks to the κ_i parameter of Eq. (16). Because of that, in our case we should get a behavior in accordance with the results of Lu and Zhu.[38] We do not consider any viscoelastic attenuation effects because our PML formulation is currently designed for elastic solids only. Considering viscoelastic solids in time-domain simulations is classical in the main domain;[31,41–43] in the PML it is possible as well, see, e.g., Martin and Komatitsch[44] in the case of the strong form of the wave equation, but for the weak form further developments would be required. The horizontal distance between the source and the recording station is 30 km. The source time function is an Hanning-weighted four-period sine wave with a dominant frequency of 50 Hz (see Jensen *et al.*,[45] page 638). The modal structure of the sound field is illustrated in Fig. 2. The dotted black and red lines, respectively, represent the modal phase velocities and modal group velocities as a function of frequency, while the solid black line represents the normalized amplitude of the source spectrum. There are four propagative modes within the band of the emitted signal, the fourth being excited very close to its cutoff frequency.

The signal received calculated with the OASES (Ref. 46) software package, which is based on wavenumber integration, is plotted in Fig. 3. This signal may be seen as the superposition of two signals: one very long signal starting at approximately 16.5 s and ending at approximately 22.5 s, and a much shorter one arriving approximately at 20.2 s. Considering the modal group velocities given in Fig. 2, the short signal is clearly associated with mode 1 while the long signal is mainly associated with mode 4. The structure of the long signal is explained in details in Brekhovskikh[47] [pp. 394–395]. Its length is linked to the large variation of the modal group velocity that occurs within the band of the

TABLE I. Elastic Pekeris waveguide (Ref. 41) parameters used in our study.

Parameters	Value
Waveguide depth	100 m
Source depth	25 m
Recording station depth	20 m
Water density	1000 kg m^{-3}
Water sound speed	1500 ms^{-1}
Sediment density	1900 kg m^{-3}
Sediment longitudinal speed	1800 ms^{-1}
Sediment shear speed	600 ms^{-1}

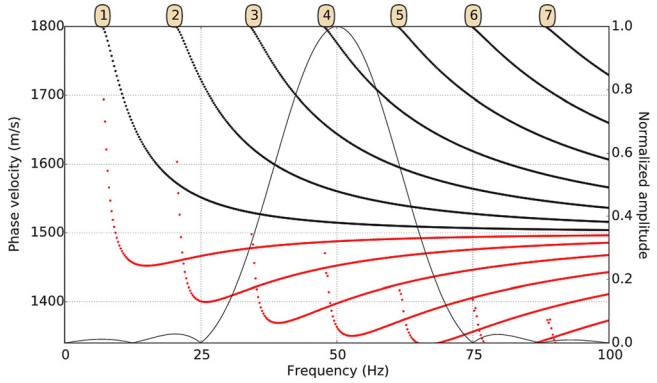

FIG. 2. (Color online) Modal dispersion curves (dotted lines) for the elastic Pekeris waveguide (Ref. 35) used in our study and frequency content of the source signal (solid line). Phase velocity curves are in black and group velocity curves are in red.

source signal for mode 4, contrary to the case of mode 1. Its left part corresponds to the signal generated when mode 4 is near its cutoff frequency. It travels at a sound speed close to the compressional speed in the sediment; it is therefore also called the "ground wave." Its right part is associated with the minimum of the modal group velocity and is also called the Airy wave. Thus, this configuration is particularly difficult to approximate because of the amount of energy that is sent near the cutoff frequency of mode 4. We should then expect discrepancies between the exact solution and the approximate one obtained with a PML at the bottom. However, before actually performing the numerical experiment it is hard to predict how the expected side effect due to the presence of the PML will affect the signal.

We now thus define a modified Pekeris model truncated with a PML. In such a configuration, the characteristics of the PML are not the only parameters that need to be analyzed. We also have to consider the influence of the size of the sediment layer, which has to be large enough in order for the waves that propagate in the water layer not to be perturbed by the PML. Even if one is only interested in propagation in the water column, there is always some energy that travels just below the water-sediment interface. The penetration depth associated with a surface wave or simply with a reflected wave (see Jensen *et al.*,[45] Fig. 8.5c) must thus be taken into account in order to avoid interferences with the absorbing layer.[48] As a consequence, the efficiency of the

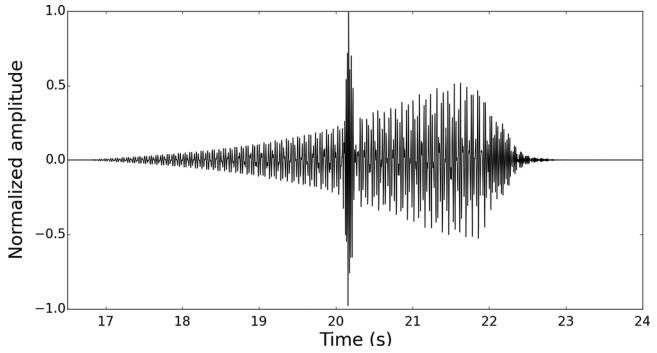

FIG. 3. Reference signal received at a distance of 30 km in our elastic Pekeris waveguide.

PML has to be studied both in terms of variations of the size of the sediment layer and of the size of the PML. Figure 4 gives the relative errors for three values of the size of the PML and two values of the size of the sediment layer. The width of the PML is given in terms of the number of mesh elements that it consists of. For clarity the reference signal is added at the bottom of the figure to be able to locate where the errors occur.

From that figure it is clear that a PML is much more efficient than a paraxial boundary condition in that context, and that it does not need to be large. One can also note that increasing the PML thickness to a value greater than three mesh elements does not reduce the relative errors. The largest relative errors are found at the beginning of the long signal that corresponds to the ground wave or equivalently to the situation in which a mode is close to its cutoff frequency, as pointed out by Lu and Zhu.[38] They can be reduced by increasing the sediment layer thickness. As a consequence, if a PML and a sediment layer are both large enough, they can efficiently replace a semi-infinite bottom. The relative errors are less than 10% for a three-element PML and a 400 m sediment layer. It should be noted that this is (purposely) the worst situation that can be encountered. For instance, if attenuation were considered in the semi-infinite sediment bottom, the part of the signal that is not accurately approximated would rapidly decrease with propagation range and the difficulties encountered in the attenuation-free model should be drastically reduced.

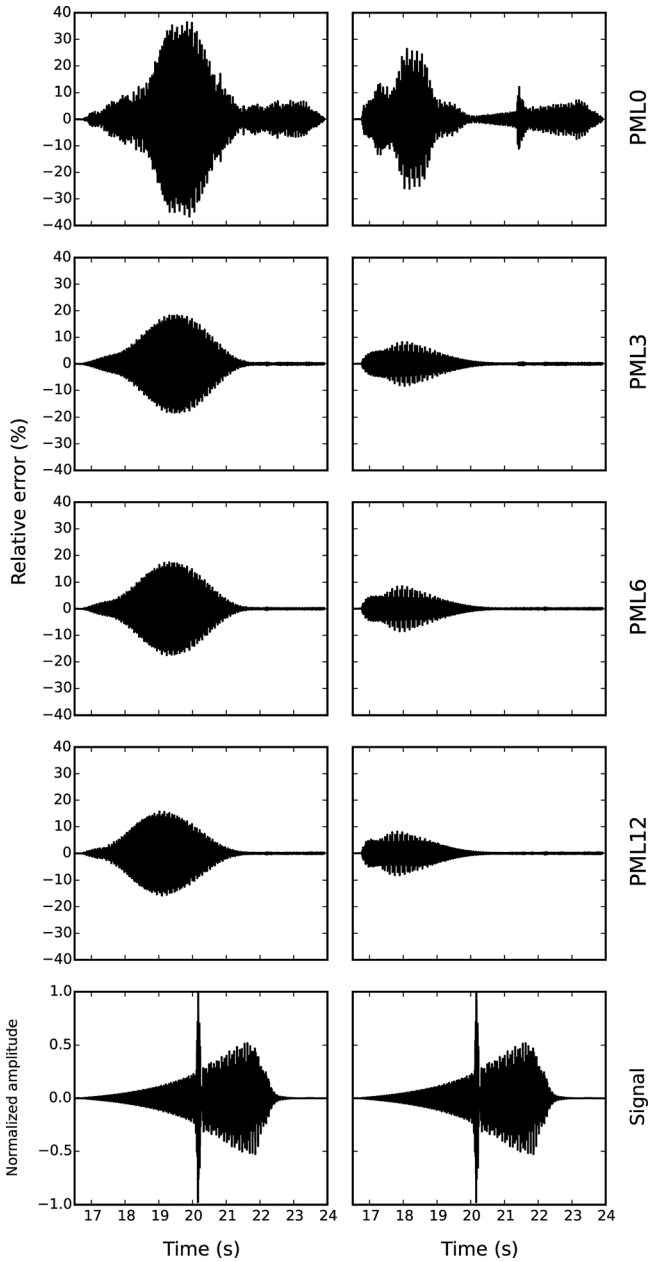

FIG. 4. Relative errors for two different sediment layer thicknesses and four PML thicknesses. The left column corresponds to a sediment layer thickness of 200 m and the right column to a sediment layer thickness of 400 m. The PML size is 0, 3, 6, 12 elements, respectively, starting from the top. In the case of a PML with a 0-element size we use a classical Stacey-type (Ref. 49) paraxial boundary condition instead. The reference signal is indicated at the bottom of each column.

B. 3D wave propagation around an elastic seamount

After studying a 2D elongated configuration, we now consider a significantly less elongated 3D domain consisting of a homogeneous water layer overlying a non-flat homogeneous elastic bottom. The physical characteristics of the water layer are unchanged compared to Sec. IV A. We choose to change the elastic properties of the bottom in order for an interface wave of Stoneley-Scholte type to be excited if a source is put close to the water-sediment interface. The new physical characteristics of the sediment are $\rho^s = 2000$ kgm^3, $c_p^s = 2400$ ms^{-1}, and $c_s^s = 1200$ ms^{-1}. The topography of the elastic bottom is (in meters)

$$z(x,y) = -400 + 100\, e^{-\left[(x-x_0)^2/2a_0^2\right]-\left[(y-y_0)^2/2b_0^2\right]} + 150\, e^{-\left[(x-x_1)^2/2a_1^2\right]-\left[(y-y_1)^2/2b_1^2\right]}, \quad (49)$$

with $x_0 = 3600$ m, $y_0 = 2400$ m, $a_0 = 300$ m, $b_0 = 525$ m, $x_1 = 3000$ m, $y_1 = 3000$ m, $a_1 = 300$ m, and $b_1 = 750$ m. We set an explosive source at $(x, y, z) = (2405, 1000, -390\,\text{m})$ with a Ricker (i.e., the second derivative of a Gaussian) source time function:

$$h(t) = A(1 - 2\pi^2 f_0^2 t^2)\, e^{-\pi^2 f_0^2 t^2} \quad (50)$$

of arbitrary amplitude $A = 10^{15}$. In order to be able to ignore the effects of thin sediment covers with very low shear speeds that would occur at high frequency in a real seamount we select a low-enough dominant frequency $f_0 = 15$ Hz; acoustic penetration into the sediment is thus several hundred meters. Because the source is located just 10 m above the bottom and because the shear wave speed is lower than the sound speed in water it will excite a strong Scholte-Stoneley interface wave.

The horizontal size of the model is 6000 m along both the x and y directions and the model extends down to a depth of 1700 m, with a free surface located at the surface of the ocean at the $z = 0$ plane. CFS-UPML absorbing layers are implemented on all the sides of the model except the free surface. The mesh is composed of 921 600 spectral elements

of polynomial degree $N = 4$ in the fluid and 3×10^6 elements in the solid, which leads to a global grid that contains 260×10^6 unique points. The PMLs occupy the three outer layers of elements of the mesh. We use a time step of 2×10^{-4} s and propagate the signal for 50 000 time steps, that is, 10 s. We consider three arrays of pressure-recording stations, each composed of three different sensors. The first array is horizontal and is situated close to the bottom, in $z = -380$ m; coordinate x is set to 1000 m while y can vary from 1000 to 5000 m. The second array is similar to the first except that it is located close to the water-air interface, in $z = -50$ m. The last array is vertical, starting close to the top of the seamount in $z = -230$ m and ending close to the water-air interface in $z = -10$ m with $(x, y) = (3000, 3000\,\text{m})$. This configuration is illustrated in Fig. 5.

We compare the solution computed with CFS-UPML to the solution obtained with a first-order Stacey-type[49] paraxial absorbing condition as well as with a reference solution computed for a very large extended model; such a solution is very expensive to compute but is exact from the point of view of mimicking an unbounded domain for a finite propagation time.

In Fig. 6 we show the relative errors between the time history of pressure recorded at the nine recording stations for a solution computed with CFS-UPML and the solution obtained with an extended domain. They agree almost perfectly, with a relative error always smaller than 4%. If the solution is computed with Stacey paraxial absorbing boundary conditions then large differences are observed, as can be seen in Fig. 7. These differences are due to the spurious reflection of body waves at grazing incidence as well as to the spurious reflection of interface waves along the ocean bottom.

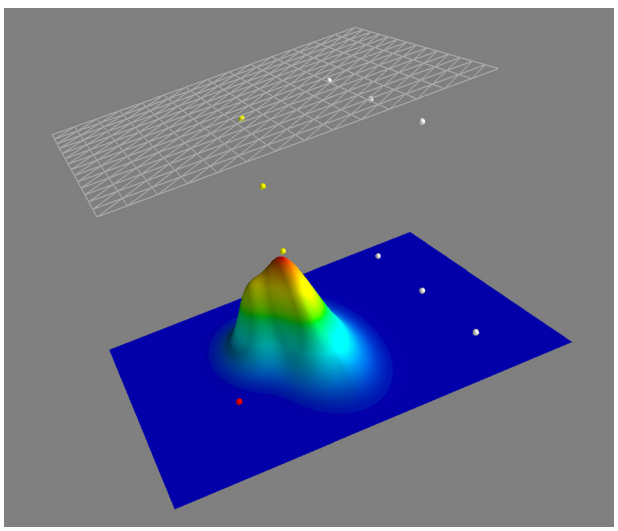

FIG. 5. (Color online) Three dimensional configuration of a seamount in shallow water used in our study. The red dot indicates the position of the source. The white dots indicate the position of recording stations belonging to two horizontal arrays, one close to the sea bottom and the other close to the sea surface. The yellow dots indicate the position of the recording stations belonging to a vertical array situated above the seamount. The horizontal size of the model is 6000 m along both the x and y directions and the distance between the sea surface and the flat part of the sea bottom is 400 m. The vertical scale is amplified by a factor of 10 here for visualization purposes.

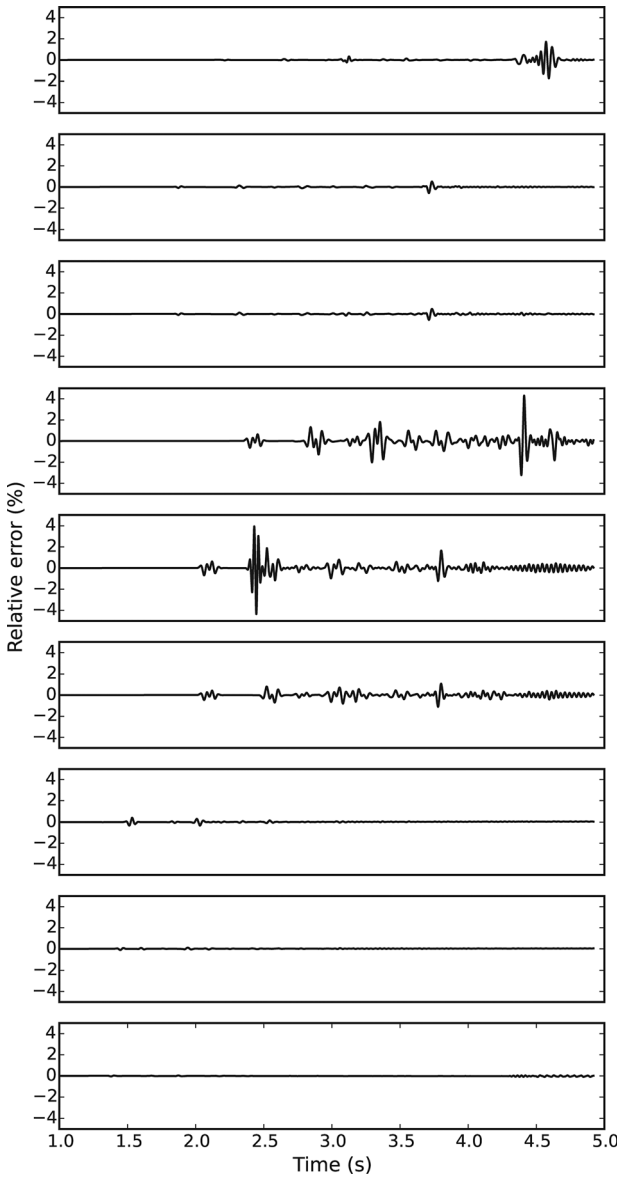

FIG. 6. Relative errors between the pressure time history recorded at the nine recording stations for the 3D elastic seamount model of Fig. 5, with CFS-UPML and with a very large mesh used to provide a reference solution with no spurious waves coming back from its edges into the main domain. Station 1 is at the top and Station 9 is at the bottom. The relative errors are always smaller than 4%.

The above results demonstrate the high accuracy and efficiency of CFS-UPML in terms of absorbing incident body waves, including at grazing incidence, as well as interface waves along the ocean bottom for such a coupled fluid-solid model.

V. CONCLUSIONS AND FUTURE WORK

We have developed and then validated a weak formulation of the CFS-UPML for full wave simulation of coupled fluid-solid problems in an unbounded or semi-infinite domain. We have first derived the frequency-domain CFS-UPML and then its time-domain counterpart in both a convolution formulation and an ADE formulation. For the first time to our knowledge we have consistently derived the correct fluid-solid interface conditions inside the PML in the

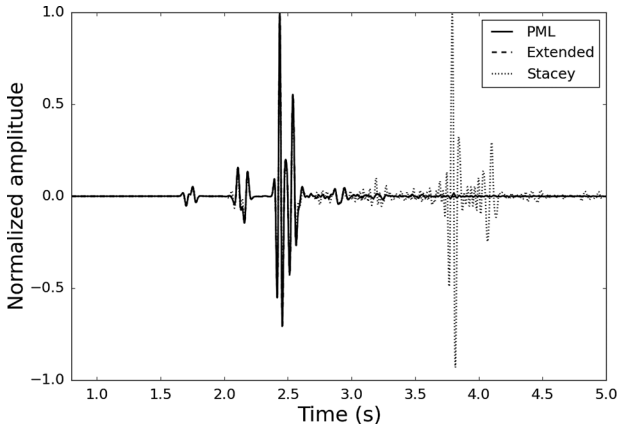

FIG. 7. Pressure time history recorded at the recording station situated in the middle of the horizontal array close to the water-air interface. Three simulations were performed: one with CFS-UPML absorbing layers (solid line), one with a very large mesh used to provide a reference solution with no spurious waves coming back into the main domain (dashed line) and one with a classical Stacey-type paraxial boundary condition (dotted line).

time domain by taking into account the effect of complex stretching and then resorting to Gauss's theorem in complex stretched coordinates. We have implemented the convolution formulation of CFS-UPML based on a Legendre SEM with explicit Newmark time integration coupled with a second-order convolution scheme, while for the ADE formulation we have used a fourth-order LDDRK scheme in order to drastically reduce numerical dispersion and dissipation, having long-range ocean acoustics wave simulations in mind.

It is worth mentioning that we have not changed the basic idea behind PML, thus for some uncommon and highly anisotropic materials our CFS-UPML formulation will be ill-posed, as the classical PML and CFS-PML are for the same anisotropic media.[50] More importantly, it is also worth mentioning that the CFS-UPML derived in this article can be applied to other numerical techniques based on the weak form of the wave equation, for instance classical finite elements or discontinuous Galerkin methods.[51,52]

One interesting point that arises from these developments and that is of interest to the underwater acoustic community is the use of a PML in the context of shallow water propagation. PMLs clearly modify the spectrum of the associated improper Sturm-Liouville problem and thus future work will be necessary to define guidelines to help choose the thickness of a sediment layer when using PMLs in the context of guided waves.

We think that future work should also address inverse (imaging) problems in addition to forward wave propagation problems, i.e., fitting our current CFS-UPML into full waveform inversion,[53–55] which have begun to gain interest in the underwater acoustics community. Another topic of interest would be extending the CFS-UPML to viscoacoustic/viscoelastic wave simulation. Last, it would be interesting to address the issue of performing a detailed accuracy analysis for CFS-UPML to find optimized profiles for the parameters used in the CFS-type coordinate transform function.[56,57]

All the developments presented have been integrated into our widely used open-source software package SPECFEM, which can be freely downloaded from the Computational Infrastructure for Geodynamics at www.geodynamics.org.

ACKNOWLEDGMENTS

We thank Ushnish Basu and Ole Sigmund for fruitful discussions. We also thank two anonymous reviewers for useful comments that improved the manuscript. Part of this work was funded by the Simone and Cino del Duca/Institut de France/French Academy of Sciences Foundation under grant 095164 and by the European "Mont-Blanc: European scalable and power efficient HPC platform based on low-power embedded technology" 288777 project of call FP7-ICT-2011-7. Z.X. also thanks the China Scholarship Council, Key Projects in the National Science & Technology Pillar Program during the 12th Five-year Plan Period (2015BAK17B01), the NSF of the Heilongjiang Province of China (LC201403) and NGSTSP of China (2013zx06002001-09) for financial support, and the continuous support from Professor Liao Zhenpeng. This work was also granted access to the French HPC resources of TGCC under allocations 2014-gen7165 and 2015-gen7165 made by GENCI and of the Aix-Marseille Supercomputing Mesocenter under allocations 14B013 and 15B034.

[1]P. Cristini and D. Komatitsch, "Some illustrative examples of the use of a spectral-element method in ocean acoustics," J. Acoust. Soc. Am. **131**(3), EL229–EL235 (2012).
[2]J. M. Collis, W. L. Siegmann, F. B. Jensen, M. Zampolli, E. T. Küsel, and M. D. Collins, "Parabolic equation solution of seismo-acoustics problems involving variations in bathymetry and sediment thickness," J. Acoust. Soc. Am. **123**, 51–55 (2008).
[3]Z. Xie, D. Komatitsch, R. Martin, and R. Matzen, "Improved forward wave propagation and adjoint-based sensitivity kernel calculations using a numerically stable finite-element PML," Geophys. J. Int. **198**(3), 1714–1747 (2014).
[4]J. P. Bérenger, "A perfectly matched layer for the absorption of electromagnetic waves," J. Comput. Phys. **114**(2), 185–200 (1994).
[5]J. J. Shirron and T. E. Giddings, "A finite-element model for acoustic scattering from objects near a fluid-fluid interface," Comput. Methods Appl. Mech. Eng. **196**, 279–288 (2006).
[6]M. Zampolli, A. Tesei, F. B. Jensen, N. Malm, and J. B. Blottman III, "A computationally efficient finite-element model with perfectly matched layers applied to scattering from axially symmetric objects," J. Acoust. Soc. Am. **122**(3), 1472–1485 (2007).
[7]J. Kormann, P. Cordo, and A. Prieto, "Perfectly matched layers for modelling seismic oceanography experiments," J. Sound Vib. **317**, 354–365 (2008).
[8]Q. Liu and J. Tao, "The perfectly matched layer for acoustic waves in absorptive media," J. Acoust. Soc. Am. **102**(4), 2072–2082 (1997).
[9]M. J. Isakson and N. P. Chotiros, "Finite-element modeling of reverberation and transmission loss in shallow water waveguides with rough boundaries," J. Acoust. Soc. Am. **129**, 1273–1279 (2011).
[10]M. Zampolli, M. J. J. Nijhof, C. A. F. de Jong, M. A. Ainslie, E. H. W. Jansen, and B. A. J. Quesson, "Validation of finite element computations for the quantitative prediction of underwater noise from impact pile driving," J. Acoust. Soc. Am. **133**, 72–81 (2013).
[11]P. J. Matuszyk and L. F. Demkowicz, "Parametric finite elements, exact sequences and perfectly matched layers," Comput. Mech. **51**(1), 35–45 (2013).
[12]P. J. Matuszyk, L. F. Demkowicz, and C. Torres-Verdin, "Solution of coupled acoustic-elastic wave propagation problems with anelastic attenuation using automatic *hp*-adaptivity," Comput. Methods Appl. Mech. Eng. **213–216**, 299–313 (2012).
[13]D. C. Calvo, K. E. Rudd, M. Zampolli, W. M. Sanders, and L. D. Bibee, "Simulation of acoustic scattering from an aluminum cylinder near a

rough interface using the elastodynamic finite integration technique," Wave Motion **47**, 616–634 (2010).
[14]W. Zhang and Y. Shen, "Unsplit complex frequency-shifted PML implementation using auxiliary differential equations for seismic wave modeling," Geophysics **75**(4), T141–T154 (2010).
[15]L. D. Landau and E. M. Lifshitz, *Fluid Mechanics* (Pergamon, New York, 1959), 536 pp.
[16]W. C. Chew and W. H. Weedon, "A 3-D perfectly matched medium from modified Maxwell's equations with stretched coordinates," Microwave Opt. Technol. Lett. **7**(13), 599–604 (1994).
[17]M. Kuzuoglu and R. Mittra, "Frequency dependence of the constitutive parameters of causal perfectly matched anisotropic absorbers," IEEE Microwave Guided Wave Lett. **6**(12), 447–449 (1996).
[18]M. Perdigao Do Carmo, *Differential Geometry of Curves and Surfaces* (Prentice-Hall, Englewood Cliffs, NJ, 1976), 503 pp.
[19]R. Matzen, "An efficient finite-element time-domain formulation for the elastic second-order wave equation: A non-split complex frequency-shifted convolutional PML," Int. J. Numer. Methods Eng. **88**(10), 951–973 (2011).
[20]I. Harari and U. Albocher, "Studies of FE/PML for exterior problems of time-harmonic elastic waves," Comput. Methods Appl. Mech. Eng. **195**(29), 3854–3879 (2006).
[21]Y. F. Li and O. Bou Matar, "Convolutional perfectly matched layer for elastic second-order wave equation," J. Acoust. Soc. Am. **127**, 1318–1327 (2010).
[22]F. Collino and C. Tsogka, "Application of the PML absorbing layer model to the linear elastodynamic problem in anisotropic heterogeneous media," Geophysics **66**(1), 294–307 (2001).
[23]W. C. Chew, J. M. Jin, and E. Michielssen, "Complex coordinate stretching as a generalized absorbing boundary condition," Microwave Opt. Technol. Lett. **15**(6), 363–369 (1997).
[24]B. Kaltenbacher, M. Kaltenbacher, and I. Sim, "A modified and stable version of a perfectly matched layer technique for the 3-D second-order wave equation in time domain with an application to aeroacoustics," J. Comput. Phys. **235**, 407–422 (2013).
[25]R. J. Luebbers and F. Hunsberger, "FDTD for Nth-order dispersive media," IEEE Trans. Antennas Propag. **40**(11), 1297–1301 (1992).
[26]T. Rylander and J.-M. Jin, "Perfectly matched layer for the time domain finite element method," J. Comput. Phys. **200**, 238–250 (2004).
[27]S. Wang, R. Lee, and F. L. Teixeira, "Anisotropic-medium PML for vector FETD with modified basis functions," IEEE Trans. Antennas Propag. **54**(1), 20–27 (2006).
[28]S. D. Gedney and B. Zhao, "An auxiliary differential equation formulation for the complex-frequency shifted PML," IEEE Trans. Antennas Propag. **58**(3), 838–847 (2010).
[29]R. Martin, D. Komatitsch, S. D. Gedney, and É. Bruthiaux, "A high-order time and space formulation of the unsplit perfectly matched layer for the seismic wave equation using auxiliary differential equations (ADE-PML)," Comput. Model. Eng. Sci. **56**(1), 17–42 (2010).
[30]J. Berland, C. Bogey, and C. Bailly, "Low-dissipation and low-dispersion fourth-order Runge-Kutta algorithm," Comput. Fluids **35**, 1459–1463 (2006).
[31]D. Komatitsch and J. Tromp, "Introduction to the spectral-element method for 3-D seismic wave propagation," Geophys. J. Int. **139**(3), 806–822 (1999).
[32]J. Tromp, D. Komatitsch, V. Hjörleifsdóttir, Q. Liu, H. Zhu, D. Peter, E. Bozdağ, D. McRitchie, P. Friberg, C. Trabant, and A. Hutko, "Near real-time simulations of global CMT earthquakes," Geophys. J. Int. **183**(1), 381–389 (2010).
[33]E. Chaljub and B. Valette, "Spectral element modelling of three-dimensional wave propagation in a self-gravitating Earth with an arbitrarily stratified outer core," Geophys. J. Int. **158**, 131–141 (2004).
[34]S. D. Gedney, "The perfectly matched layer absorbing medium," in *Advances in Computational Electrodynamics: The Finite-Difference Time-Domain Method*, edited by Allen Taflove (Artech House, Boston, MA, 1998), Chap. 5, pp. 263–343.
[35]C. L. Pekeris, "Theory of explosion of sound in shallow water," Geol. Soc. Am. Mem. **27**, 1–117 (1948).
[36]F. Press and M. Ewing, "Propagation of explosive sound in a liquid layer over-lying a semi-infinite elastic solid," Geophysics **15**(3), 426–446 (1950).
[37]F. Olyslager, "Discretization of continuous spectra based on perfectly matched layers," SIAM J. Appl. Math. **64**(4), 1408–1433 (2004).
[38]Y. Y. Lu and J. Zhu, "Perfectly matched layer for acoustic waveguide modeling—Benchmark calculations and perturbation analysis," Comput. Model. Eng. Sci. **22**(3), 235–248 (2007).
[39]J. Zhu and Y. Y. Lu, "Asymptotic solutions of the leaky modes and PML modes in a Pekeris waveguide," Wave Motion **45**(3), 207–216 (2008).
[40]J. Zhu and Z. Chen, "On the validity of modal expansion in Pekeris waveguide with PML," J. Appl. Comput. Math. **2**, 124–127 (2013).
[41]É. Blanc, D. Komatitsch, E. Chaljub, B. Lombard, and Z. Xie, "Highly accurate stability-preserving optimization of the Zener viscoelastic model, with application to wave propagation in the presence of strong attenuation," Geophys. J. Int. **205**(1), 427–439 (2016).
[42]J. M. Carcione, D. Kosloff, and R. Kosloff, "Wave propagation simulation in a linear viscoelastic medium," Geophys. J. Int. **95**, 597–611 (1988).
[43]P. Moczo and J. Kristek, "On the rheological models used for time-domain methods of seismic wave propagation," Geophys. Res. Lett. **32**, L01306, doi:10.1029/2004GL021598 (2005).
[44]R. Martin and D. Komatitsch, "An unsplit convolutional perfectly matched layer technique improved at grazing incidence for the viscoelastic wave equation," Geophys. J. Int. **179**(1), 333–344 (2009).
[45]F. B. Jensen, W. Kuperman, M. Porter, and H. Schmidt, *Computational Ocean Acoustics*, 2nd ed. (Springer-Verlag, Berlin, 2011), 794 pp.
[46]H. Schmidt *OASES Version 3.1 User Guide and Reference Manual* (Center for Ocean Engineering, Massachusetts Institute of Technology, Boston, MA, 2004). Available at acoustics.mit.edu/faculty/henrik/oases.html.
[47]L. M. Brekhovskikh, *Waves in Layered Media* (Academic, New York, 1960), 574 pp.
[48]G. Festa, E. Delavaud, and J. P. Vilotte, "Interaction between surface waves and absorbing boundaries for wave propagation in geological basins: 2D numerical simulations," Geophys. Res. Lett. **32**(20), L20306, doi:10.1029/2005GL024091 (2005).
[49]R. Stacey, "Improved transparent boundary formulations for the elastic wave equation," Bull. Seism. Soc. Am. **78**(6), 2089–2097 (1988).
[50]E. Bécache, S. Fauqueux, and P. Joly, "Stability of perfectly matched layers, group velocities and anisotropic waves," J. Comput. Phys. **188**(2), 399–433 (2003).
[51]M. Käser and M. Dumbser, "A highly accurate discontinuous Galerkin method for complex interfaces between solids and moving fluids," Geophysics **73**(3), T23–T35 (2008).
[52]L. C. Wilcox, G. Stadler, C. Burstedde, and O. Ghattas, "A high-order discontinuous Galerkin method for wave propagation through coupled elastic-acoustic media," J. Comput. Phys. **229**(24), 9373–9396 (2010).
[53]A. Fathi, L. F. Kallivokas, and B. Poursartip, "Full-waveform inversion in three-dimensional PML-truncated elastic media," Comput. Methods Appl. Mech. Eng. **296**, 39–72 (2015).
[54]V. Monteiller, S. Chevrot, D. Komatitsch, and Y. Wang, "Three-dimensional full waveform inversion of short-period teleseismic wavefields based upon the SEM-DSM hybrid method," Geophys. J. Int. **202**(2), 811–827 (2015).
[55]J. Tromp, D. Komatitsch, and Q. Liu, "Spectral-element and adjoint methods in seismology," Commun. Comput. Phys. **3**(1), 1–32 (2008).
[56]N. Feng, Y. Yue, C. Zhu, L. Wan, and Q. H. Liu, "Second-order PML: Optimal choice of *n*th-order PML for truncating FDTD domains," J. Comput. Phys. **285**, 71–83 (2015).
[57]K. Sagiyama, S. Govindjee, and P.-O. Persson, "An efficient time-domain perfectly matched layers formulation for elastodynamics on spherical domains," Int. J. Numer. Methods Eng. **100**(6), 419–441 (2014).